Journal of Materials Chemistry C

ROYAL SOCIETY OF CHEMISTRY

PAPER

View Article Online
View Journal | View Issue

Cite this: J. Mater. Chem. C, 2026, 14, 5423

Development of high-efficiency near-infrared organic light-emitting diodes using TPA-DCPP *via* interface exciplex formation

Cheng-Yen Chuang,[a] Bishal Paul,[b] Jhih-Yu Ke,[a] Sih-Han Ji,[a] Sheng-Yuan Chu *[ab] and Po-Ching Kao[c]

Received 30th November 2025,
Accepted 22nd January 2026

DOI: 10.1039/d5tc04226g

rsc.li/materials-c

Near-infrared organic light-emitting diodes (NIR OLEDs) hold great promise for applications in biomedical imaging, optical communication, and night-vision technologies. However, their efficiencies remain limited by the intrinsically narrow bandgaps of NIR emitters and severe aggregation-caused quenching (ACQ). Here, a high-efficiency NIR OLED is demonstrated using an interfacial exciplex formed between CBP and PO-T2T as an energy-transfer medium to sensitize the NIR emitter TPA-DCPP. This interfacial exciplex strategy avoids the use of heavy-metal complexes and complex thermally activated delayed fluorescence molecular design, enabling a heavy-metal-free and structurally simple device concept. The exciplex exhibits efficient Förster resonance energy transfer (FRET) to the guest emitter due to the strong spectral overlap between its emission and the TPA-DCPP absorption band. Through systematic optimization of the device architecture—including transport-layer thickness and guest-doping concentration—the optimized OLED achieves a maximum external quantum efficiency (EQE_{max}) of 15.2% and a peak luminance of 2152 cd m^{-2} at 700 nm. This work highlights the effectiveness of interfacial exciplex-mediated energy transfer in mitigating ACQ-induced efficiency losses, providing a straightforward and reproducible pathway toward high-performance, heavy-metal-free NIR OLEDs.

1. Introduction

Organic light-emitting diodes (OLEDs) have been extensively studied for display and lighting technologies owing to their high brightness, wide viewing angles, and mechanical flexibility. Among different emission regions, near-infrared (NIR) OLEDs have garnered growing interest for specialized applications in optical communication, night-vision displays, and biomedical imaging.[1–4] However, achieving high efficiency in NIR OLEDs remains a persistent challenge because the small bandgaps of NIR emitters promote non-radiative decay and aggregation-caused quenching (ACQ), resulting in severe efficiency losses.[5–9] Recent strategies to enhance NIR OLED performance have focused on the development of thermally activated delayed fluorescence (TADF) emitters and heavy-metal complexes to harvest triplet excitons. Although TADF materials can utilize triplet excitons without the need for metals, their complex synthesis routes and limited chemical stability hinder large-scale application.[10–12] In contrast, heavy-metal complexes provide high efficiency but are costly and raise environmental concerns.[13] Therefore, a simple and effective approach that enables efficient triplet utilization while maintaining facile fabrication is highly desirable.

Exciplex systems, generated through intermolecular charge transfer between donor and acceptor molecules, offer a promising pathway to address these limitations.[14–17] They exhibit intrinsic reverse intersystem crossing (RISC) characteristics similar to TADF materials and can be readily formed *via* molecular blending without complex chemical modification.[14] Notably, interfacial exciplexes can act as efficient energy-transfer bridges to sensitize guest emitters when sufficient spectral overlap is present.[18] In this work, an interfacial exciplex-based NIR OLED is demonstrated using CBP (donor) and PO-T2T (acceptor) as the exciplex pair to transfer excitonic energy to the NIR emitter TPA-DCPP. Through systematic optimization of the transport-layer thickness and guest-doping concentration, the device achieves efficient energy transfer and balanced carrier recombination, delivering a maximum external

[a] Department of Electrical Engineering, National Cheng Kung University, Tainan, 70101, Taiwan, Republic of China. E-mail: chusy@mail.ncku.edu.tw; Fax: +886 6 2345482; Tel: +886 6 2757575x62381
[b] Department of Program on Semiconductor Manufacturing Technology (PSMT), Academy of Innovative Semiconductor and Sustainable Manufacturing (AISSM), National Cheng Kung University, Tainan, 70101, Taiwan, Republic of China
[c] Department of Electrophysics, National Chiayi University, Chiayi, 60004, Taiwan, Republic of China

quantum efficiency (EQE_{max}) of 15.2% and a peak luminance of 2152 cd m^{-2}. This study establishes a straightforward and reproducible device architecture that leverages interfacial exciplex-mediated energy transfer to realize high-efficiency NIR emission, providing a practical and cost-effective alternative to complex TADF or phosphorescent systems. Compared with conventional thermally activated delayed fluorescence emitters and heavy-metal complexes, the interfacial exciplex strategy employed here offers advantages in terms of simple device fabrication and high device performance.

2. Results and discussion

2.1 Photoluminescence and absorption characteristics of the host, guest, and exciplex in NIR OLEDs

Fig. 1 displays the normalized absorption spectra of TPA-DCPP, CBP, and PO-T2T, together with the photoluminescence (PL) spectra of CBP, PO-T2T, and their exciplex blend CBP : PO-T2T (1 : 1).

This measurement serves two purposes. First, it reveals the spectral overlap between the exciplex (CBP:PO-T2T) emission and the guest emitter (TPA-DCPP) absorption, which is essential for Förster resonance energy transfer (FRET). Efficient FRET occurs only when substantial overlap exists between the donor emission and the acceptor absorption spectra. In this case, the CBP:PO-T2T exciplex exhibits a PL peak at 488 nm, and its emission band overlaps strongly with the UV-vis absorption spectrum of TPA-DCPP, enabling effective excitonic energy transfer.

Second, the measurement confirms the formation of the exciplex. The PL peaks of neat CBP and PO-T2T films appear at 377 nm and 388 nm, respectively. Upon co-deposition, the blend exhibits a distinct red-shifted PL peak at 488 nm, clearly indicating the formation of an exciplex through intermolecular charge-transfer interactions between the donor (CBP) and acceptor (PO-T2T).

Notably, only exciplex emission is observed in the CBP:PO-T2T blend, with no discernible residual emission from the locally excited states of CBP or PO-T2T. This behavior arises because the exciplex state possesses a significantly lower emission energy than the excited states of the individual donor and acceptor molecules. As a result, excitons generated upon photoexcitation of the CBP:PO-T2T film rapidly relax from the higher-energy CBP and PO-T2T excited states into the lower-energy exciplex state. Consequently, radiative recombination from the locally excited donor or acceptor states is effectively suppressed, and photoluminescence is dominated by exciplex emission.

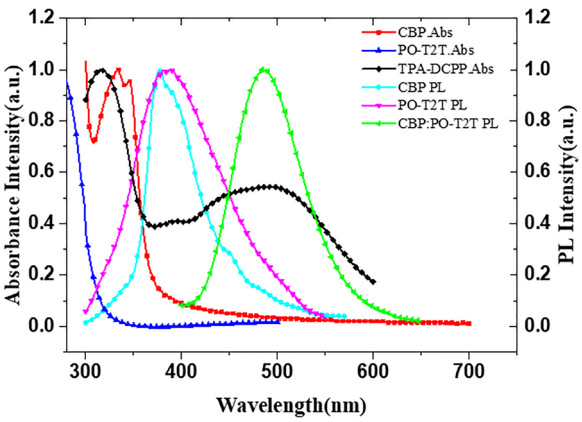

Fig. 1 Absorption spectra of TPA-DCPP, CBP, and PO-T2T, and PL spectra of CBP:PO-T2T, CBP, and PO-T2T.

In addition, exciplex emission is typically associated with characteristic excited-state dynamics, including a longer emission lifetime and the presence of delayed emission components compared with those of the individual donor or acceptor materials. Such behavior has been clearly demonstrated for CBP/PO-T2T interfacial exciplex systems,[19] where time-resolved photoluminescence measurements revealed a distinct red-shifted exciplex emission accompanied by prompt (nanosecond-scale) and delayed (microsecond-scale) decay components. These time-resolved features provide strong evidence for the formation of a charge-transfer exciplex state and support its role as an efficient energy donor for Förster resonance energy transfer (FRET) to guest emitters.

Furthermore, the intrinsic excited-state dynamics of neat CBP, including its singlet and triplet lifetimes, have been well established by a study.[20] The absence of comparable long-lived or delayed emission components in neat CBP further supports that the emission behavior observed in CBP/PO-T2T blends originates from exciplex formation rather than from the locally excited donor states.

In the present study, exciplex identification is therefore based on the emergence of a new red-shifted steady-state PL emission band that is absent in the neat CBP and PO-T2T films, together with its demonstrated role as an effective energy-transfer donor to TPA-DCPP, rather than on direct PLQY measurements.

CBP functions as an electron donor and PO-T2T as an electron acceptor, enabling efficient intermolecular charge transfer at their interface and resulting in the formation of a charge-transfer exciplex state with an emission energy lower than the locally excited states of the individual materials. The emission energy of this exciplex exhibits strong spectral overlap with the absorption band of TPA-DCPP, providing the physical basis for efficient Förster resonance energy transfer from the exciplex to the NIR guest emitter.

To further clarify the energy transfer pathway, the highest occupied molecular orbital (HOMO) and lowest unoccupied molecular orbital (LUMO) energy levels of all materials involved in this work are summarized, and a corresponding energy level diagram is provided (Fig. 2). As shown in the diagram, the relative alignment of the HOMO and LUMO levels of CBP and PO-T2T facilitates intermolecular charge transfer at their interface, enabling exciplex formation. Moreover, the energy levels of the resulting exciplex state are well matched with those of the NIR emitter TPA-DCPP, allowing efficient excitonic energy transfer from the exciplex to TPA-DCPP. This favorable energy-level alignment provides a clear physical basis for the observed exciplex-mediated Förster resonance energy transfer and the

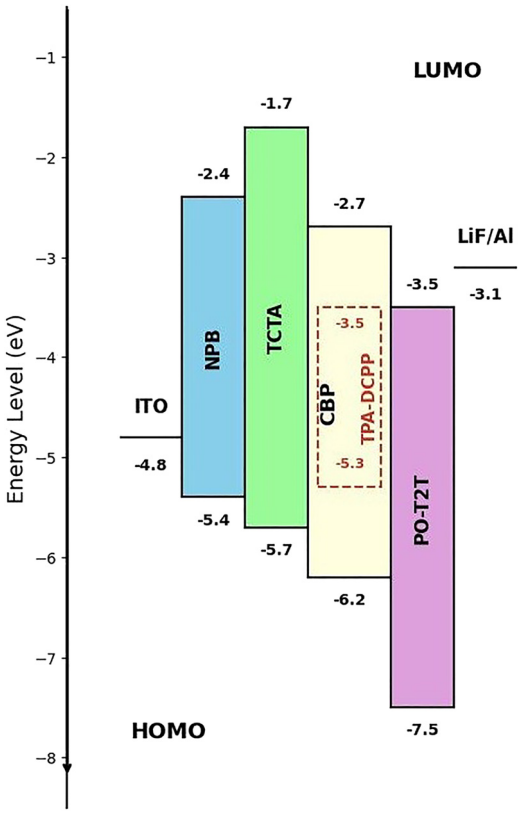

Fig. 2 Energy band diagram (HOMO and LUMO) of the materials.

resulting efficient near-infrared emission. Based on Fig. 2, the formation mechanism of the exciplex suggests that an interfacial exciplex between CBP (donor) and PO-T2T (acceptor) was formed, followed by Förster resonance energy transfer (FRET) from the exciplex to the TPA-DCPP molecules, which ultimately results in efficient near-infrared emission from TPA-DCPP. In addition, by appropriately adjusting the thicknesses of NPB (HTL) and PO-T2T (ETL), balanced hole and electron injection is achieved. This balance effectively confines the recombination zone to the CBP/PO-T2T interface, thereby enhancing exciplex formation and improving the efficiency of exciplex-mediated energy transfer.

2.2 Transmittance spectra of EML with different guest-doping concentrations

By adjusting different doping concentrations of CBP:TPA-DCPP thin films, transmittance spectra were recorded to investigate whether varying doping concentrations would significantly affect the photon output.[21] Since the magnitude of photon output directly influences the efficiency of subsequently fabricated devices, this measurement serves as an important basis for the experiment.[22,23]

As shown in Fig. 3, the average optical transmittance within the visible range remains above 93% for all doping concentrations. Therefore, in this study, the doping of TPA-DCPP does not cause a significant impact on the photon output, indicating negligible influence on the device's electroluminescence efficiency.

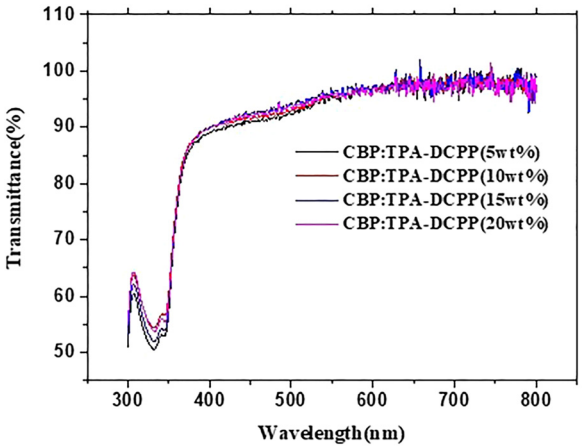

Fig. 3 Transmittance spectra of the emitting layer (EML) with different doping concentrations of TPA-DCPP.

2.3 Contact-angle measurements and surface-energy analysis of the emissive layer with different guest-doping concentrations

The influence of different concentrations of the near-infrared (NIR) guest emitter TPA-DCPP doped into the CBP host on the surface properties of the resulting films was systematically investigated. Because interfacial interactions strongly affect device performance, contact angles between deposited droplets and film surfaces were measured using a contact-angle goniometer to determine the surface energy and polarity of the films.[18] CBP:TPA-DCPP films with doping concentrations of 5, 10, 15, and 20 wt% were examined. Deionized (DI) water and diiodomethane (CH_2I_2) served as the testing liquids, and the sessile-drop method was employed for all measurements.

The contact angles of CBP:TPA-DCPP (X wt%) films measured with DI water are shown in Fig. 4(a–d), with values of 97.69°, 93.91°, 89.72°, and 95.86°, respectively. When measured with diiodomethane, the contact angles shown in Fig. 5(a–d) were 63.45°, 57.70°, 52.89°, and 58.48°, respectively. These

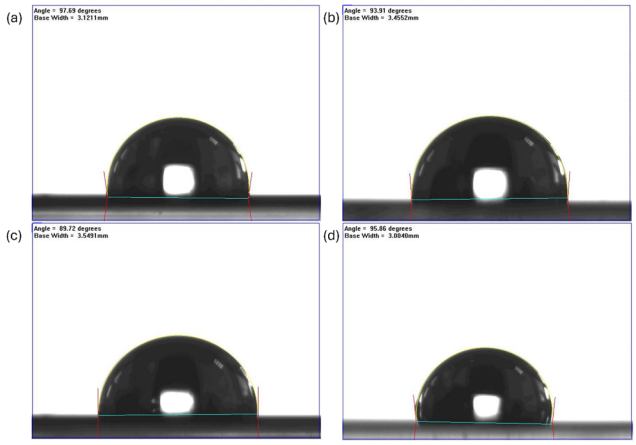

Fig. 4 The contact angles of deionized water were measured on CBP:TPA-DCPP thin films with doping concentrations of 5 wt%, 10 wt%, 15 wt%, and 20 wt%, respectively.

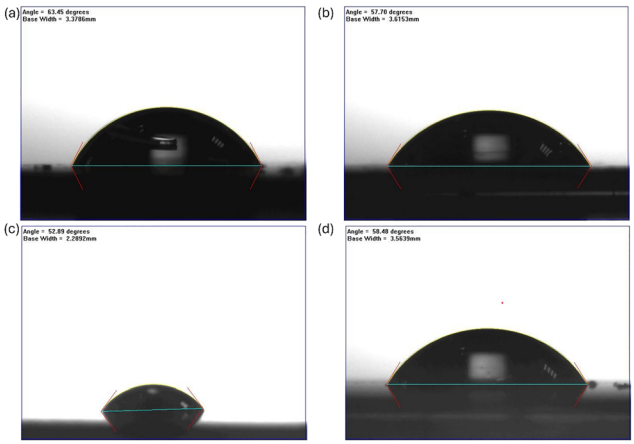

Fig. 5 The contact angles of diiodomethane were measured on CBP:TPA-DCPP thin films with doping concentrations of 5 wt%, 10 wt%, 15 wt%, and 20 wt%, respectively.

measured contact angles were substituted into eqn (1) to calculate the surface energy and surface polarity, as summarized in Fig. 6 and Table 2.

For the CBP:TPA-DCPP (5 wt%) film, the surface energy and surface polarity were determined to be 27.82 mJ m^{-2} and 0.038, respectively. As the TPA-DCPP concentration increased to 15 wt%, the surface energy and polarity rose to 34.99 mJ m^{-2} and 0.052, respectively. This increase suggests that higher guest doping enhances intermolecular interactions between CBP and TPA-DCPP molecules, leading to modified film morphology and stronger interfacial bonding.[24] However, when the doping concentration reaches 20 wt%, the surface energy decreases slightly, likely due to the emergence of surface defects at excessive guest loading. Higher surface energy and polarity reflect stronger interfacial cohesion between the layers, which in this study facilitates more effective exciplex formation.

2.4 Photoluminescence spectra of the emissive layer with different guest-doping concentrations

The photoluminescence (PL) spectra of CBP:TPA-DCPP (*X* wt%) films with neat TPA-DCPP and varying doping concentrations (*X* = 5, 10, 15, and 20) are presented in Fig. 7. The PL

Table 1 Surface tension and components of the test solution

Surface tension (mN m^{-1})	γ_L^p	γ_L^d	γ_L
H_2O	51.0	21.8	72.8
CH_2I_2	2.3	48.5	50.8

characteristics provide insights into the energy-transfer efficiency, concentration quenching, and intermolecular interactions within the emissive layer.

As shown in Fig. 7, the PL intensities of the 5 wt% and 10 wt% films are relatively weak, which can be attributed to the low concentration of the guest emitter TPA-DCPP. At these lower doping levels, most of the emission originates from the CBP host, indicating limited energy transfer efficiency and, consequently, reduced PL intensity. When the doping concentration increases to 15 wt%, energy transfer from the host to the guest becomes more efficient, leading to dominant guest emission and the highest observed PL intensity. However, a further increase to 20 wt% results in enhanced concentration quenching, thereby reducing PL intensity. These findings suggest that a doping concentration of 15 wt% provides the optimal balance between energy transfer and exciton quenching. Although PL spectra alone may not be sufficient to unambiguously identify exciplex emission, Colella *et al.*[25] employed PLQY measurements, together with PL and time-resolved spectroscopy, to verify exciplex emission and correlate its efficiency with ΔE_{ST} and RISC processes. They have confirmed that the CBP:PO-T2T blend forms the exciplex. Further confirmation of this behavior will be discussed in the subsequent device performance analysis.

It is evident from Fig. 7 that the PL peak of TPA-DCPP is significantly red-shifted relative to the CBP:TPA-DCPP blended films at lower doping concentrations. At low doping levels, TPA-DCPP molecules are well dispersed within the CBP host matrix, resulting in relatively blue-shifted emission. As the TPA-DCPP doping concentration increases, a systematic redshift of the PL peak is observed, which can be attributed to enhanced intermolecular interactions among TPA-DCPP molecules as the average intermolecular distance decreases. These solid-state effects modify the emissive environment, leading to a gradual redshift of the emission toward that of the neat TPA-DCPP film.

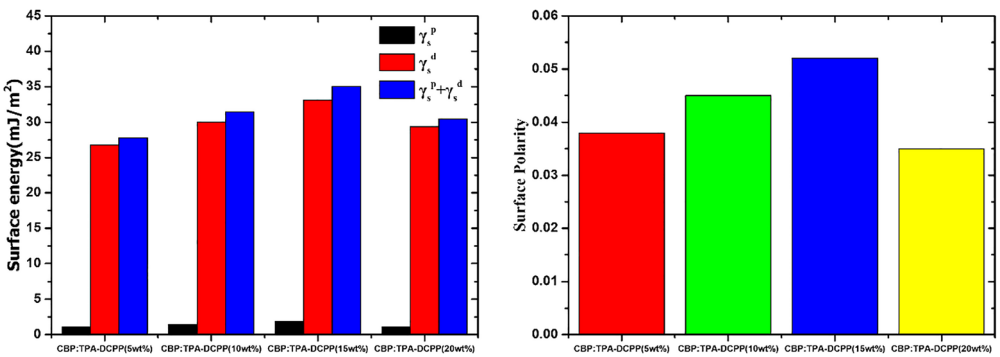

Fig. 6 Surface energy (left) and surface polarity (right) of CBP:TPA-DCPP films with doping concentrations of 5 wt%, 10 wt%, 15 wt%, and 20 wt%, respectively.

Table 2 Results of contact angle measurements using deionized water and diiodomethane, and calculations of surface energy and surface polarity

	Water angle	CH_2I_2 angle	Surface energy	Surface polarity	γ_s^p	γ_s^d	$\gamma_s^p + \gamma_s^d$
CBP:TPA-DCPP (5 wt%)	97.69	63.45	27.82	0.038	1.06	26.76	27.82
CBP:TPA-DCPP (10 wt%)	93.91	57.70	31.47	0.045	1.42	30.05	31.47
CBP:TPA-DCPP (15 wt%)	89.72	52.89	34.99	0.052	1.85	33.14	34.99
CBP:TPA-DCPP (20 wt%)	95.86	58.48	30.50	0.035	1.09	29.41	30.50

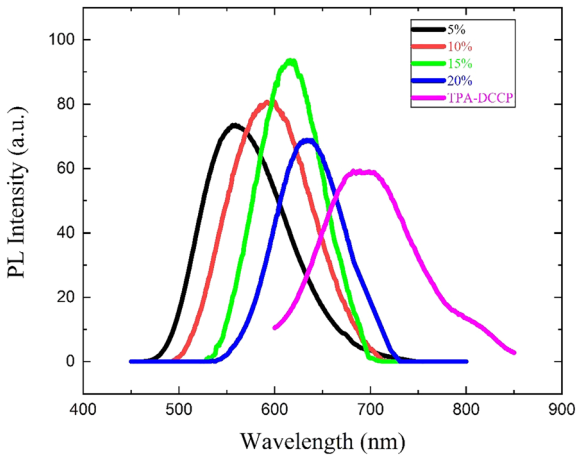

Fig. 7 Photoluminescence spectra of CBP:TPA-DCPP films with different doping concentrations.

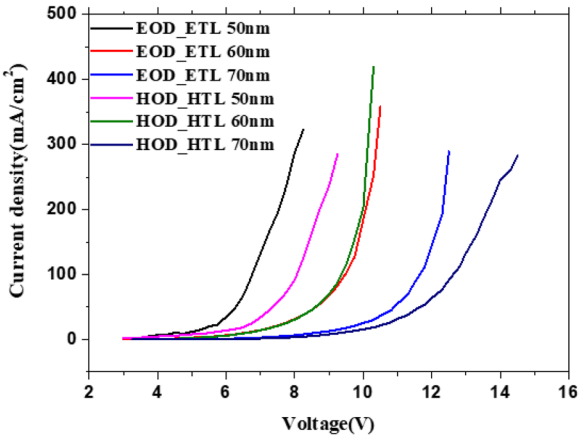

Fig. 9 *J*–*V* (current density–voltage) characteristics of single-carrier near-infrared OLED devices.

At the highest doping concentration (20 wt%), the PL spectrum approaches the emission characteristics of TPA-DCPP, indicating a transition toward guest-dominated emission. However, excessive aggregation at high concentrations also introduces concentration quenching, consistent with the reduced PL intensity observed. Overall, the observed doping-dependent spectral evolution supports the interpretation that the emission peak shift arises from changes in the molecular environment and intermolecular interactions as a function of guest concentration.

2.5 Optimization of single-carrier devices for balanced carrier transport

Single-carrier devices were fabricated to determine the optimal parameters for achieving balanced carrier transport within the emissive layer. By adjusting the thicknesses of the hole-transport layer (HTL) and electron-transport layer (ETL), the carrier recombination zone can be precisely controlled to maximize device efficiency. Accordingly, two types of single-carrier devices—hole-only devices (HODs) and electron-only devices (EODs)—were fabricated, as illustrated in Fig. 8.

HODs were constructed by replacing the ETL with the HTL material to function as a hole-blocking layer, whereas the reverse configuration yielded EODs. The device structures were as follows:

Electron-only devices: ITO/PO-T2T (20 nm)/TCTA (5 nm)/CBP (10 nm)/CBP:TPA-DCPP (10 wt%, 10 nm)/PO-T2T (Y nm)/LiF (1 nm)/Al (100 nm).

Hole-only devices: ITO/NPB (*X* nm, *X* = 50, 60, 70)/TCTA (5 nm)/CBP (10 nm)/CBP:TPA-DCPP (10 wt%, 10 nm)/PO-T2T (20 nm)/NPB (20 nm)/LiF (1 nm)/Al (100 nm).

As shown in Fig. 9, the optimal configuration was achieved when both the HTL and ETL thicknesses were 60 nm. Under

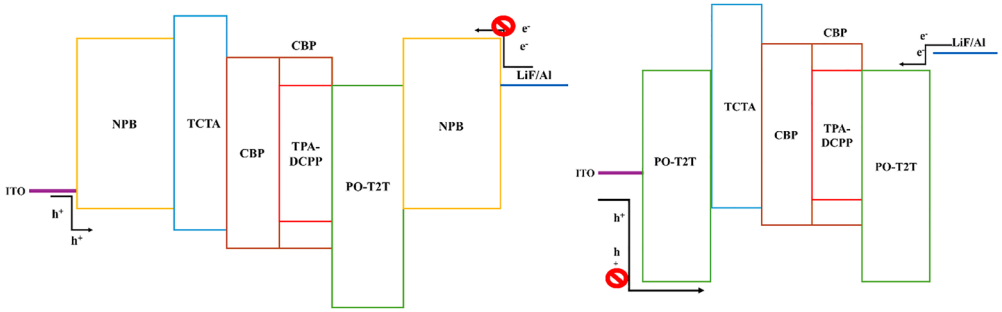

Fig. 8 Schematic illustration of carrier transport in single-carrier NIR OLED devices: HOD (left) and EOD (right).

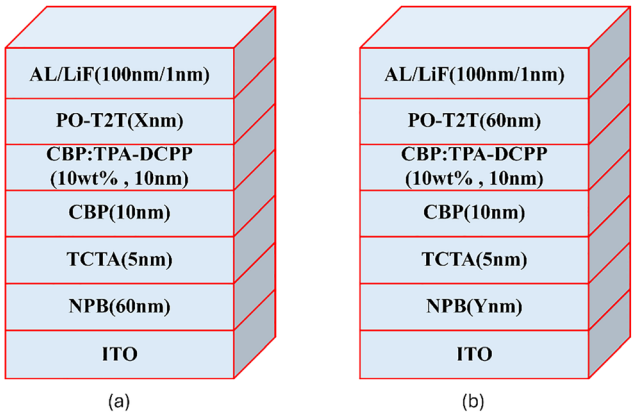

Fig. 10 Schematic diagrams of device structures with different transport layer thicknesses: (a) different ETL thicknesses and (b) different HTL thicknesses.

these conditions, the device exhibited the most balanced carrier injection and transport, enabling a broader recombination zone and more efficient exciton formation. This balanced carrier transport enhances energy-transfer efficiency, ultimately leading to improved overall device performance.

From a mechanistic perspective, the exciplex state exhibits a significantly lower emission energy than CBP (donor) and PO-T2T (acceptor), and this behavior can be clearly understood from the PL emission peak positions of the three species. The exciplex emission appears at 488 nm, whereas the PL peaks of CBP and PO-T2T are located at 377 nm and 388 nm, respectively. This pronounced energy difference causes excitons generated upon photoexcitation of the CBP:PO-T2T film to rapidly relax from CBP (D) and PO-T2T (A) into the lower-energy exciplex state. As a result, photoluminescence emission from CBP (D) and PO-T2T (A) is effectively suppressed, and only exciplex emission is observed.

2.6 Optimization of transport-layer thickness in near-infrared OLEDs

Although the optimal transport-layer thicknesses were identified using single-carrier devices in the previous section, the actual optimum in complete OLEDs may differ due to the more complex charge-recombination and energy-transfer processes. Therefore, in this section, the optoelectronic performance of near-infrared (NIR) OLEDs with different transport-layer thicknesses was systematically investigated.[26]

Fig. 10a shows the device configuration with a fixed HTL thickness and varying ETL thickness. The structure was ITO/NPB (60 nm)/TCTA (5 nm)/CBP (10 nm)/CBP:TPA-DCPP (10 wt%, 10 nm)/PO-T2T (X nm, X = 50, 60, 70)/LiF (1 nm)/Al (100 nm). Fig. 10b illustrates the complementary structure, where the ETL thickness was fixed while the HTL thickness was varied, following the configuration: ITO/NPB (Y nm, Y = 50, 60, 70)/TCTA (5 nm)/CBP (10 nm)/CBP:TPA-DCPP (10 wt%, 10 nm)/PO-T2T (60 nm)/LiF (1 nm)/Al (100 nm). By adjusting the thicknesses of the HTL and ETL, the transport distances of

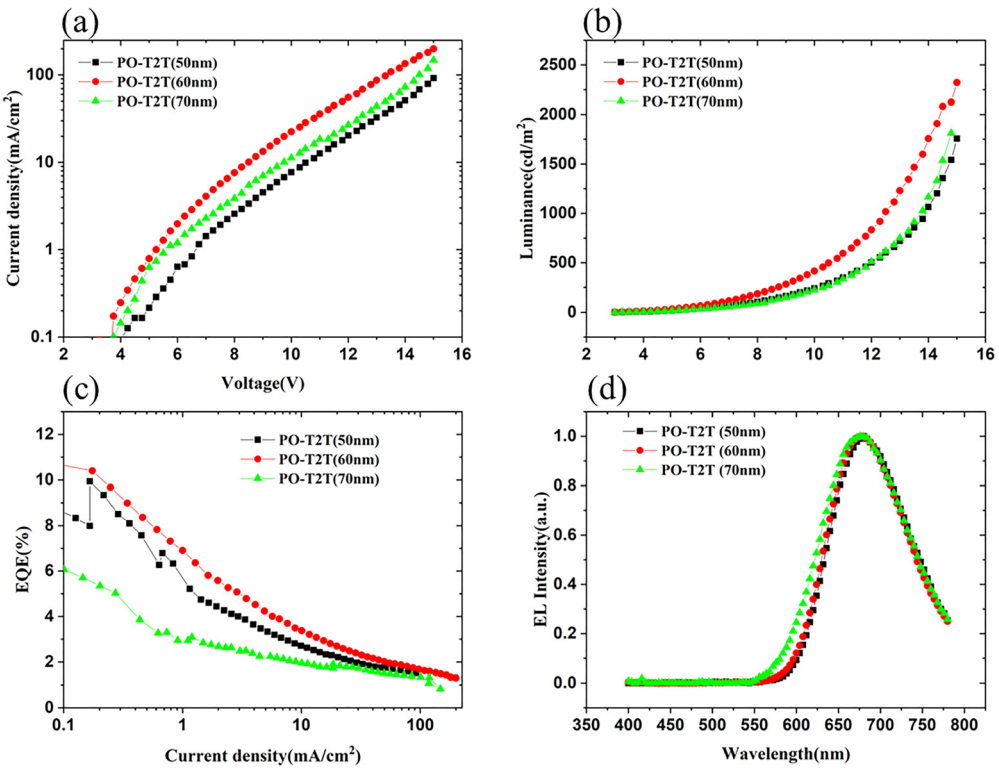

Fig. 11 Optoelectronic performance of NIR OLEDs with different PO-T2T thicknesses: (a) J–V characteristics, (b) L–V curves, (c) EQE–J curves, and (d) EL spectra.

Table 3 Comparison of optoelectronic characteristics for devices with different ETL thicknesses

ETL (nm)	L_{max} (cd m^{-2})	EQE$_{max}$ (%)	Turn on voltage (V)	EL peak (nm)
50	1758	9.34	2.75	660
60	2322	11.5	2.75	680
70	1438	7.36	2.75	676

Table 4 Comparison of optoelectronic characteristics for devices with different HTL thicknesses

HTL (nm)	L_{max} (cd m^{-2})	EQE$_{max}$ (%)	Turn on voltage (V)	EL peak (nm)
50	1049	10.0	2.75	680
60	2322	11.5	2.5	680
70	1350	8.7	2.75	680

holes and electrons were tuned, and the resulting optoelectronic characteristics were evaluated.

As shown in Fig. 11a–d and Table 3, for devices with varying ETL thicknesses, the luminance values at 50, 60, and 70 nm were 1758 cd m^{-2}, 2322 cd m^{-2}, and 1438 cd m^{-2}, respectively, while the corresponding external quantum efficiencies (EQEs) were 9.34%, 11.5%, and 7.36%. Among these, the device with a 60 nm ETL exhibited the highest luminance and optimal efficiency. Similarly, Fig. 12(a–d) and Table 4 show the *J–V*, *L–V*, EQE, and EL characteristics of devices with different NPB (HTL) thicknesses. The luminance values at 50, 60, and 70 nm were 1049 cd m^{-2}, 1350 cd m^{-2}, and 2322 cd m^{-2}, respectively, while the corresponding EQEs were 10.0%, 11.5%, and 8.7%. The 60 nm HTL device again demonstrated the highest luminance and best efficiency, indicating balanced carrier injection and efficient recombination at this thickness.

Overall, optimization of both the ETL and HTL confirms that a thickness of 60 nm for each layer yields the most balanced carrier transport and efficient exciton recombination, consistent with the trends observed in the single-carrier device analysis (Section 2.5). These results verify that the 60 nm HTL/ETL configuration provides the optimal parameters for high-performance NIR OLED operation.

2.7 Optoelectronic characteristics and efficiency performance of devices with varied guest-doping concentrations

The optoelectronic characteristics and efficiency performance of near-infrared (NIR) OLEDs incorporating different guest-doping concentrations[27] were systematically investigated. Four devices were fabricated with TPA-DCPP doping concentrations of 5, 10, 15, and 20 wt%. The device architecture, illustrated in Fig. 13, was ITO/NPB (60 nm)/TCTA (5 nm)/CBP (10 nm)/CBP:TPA-DCPP (*X* wt%, 10 nm)/PO-T2T (60 nm)/LiF (1 nm)/Al (100 nm), where *X* represents the TPA-DCPP doping ratio.

As shown in Fig. 14(a–c), increasing the doping concentration from 5 wt% to 15 wt% leads to a marked enhancement in device performance, with the external quantum efficiency (EQE) improving from 7.36% to 15.2% and the luminance

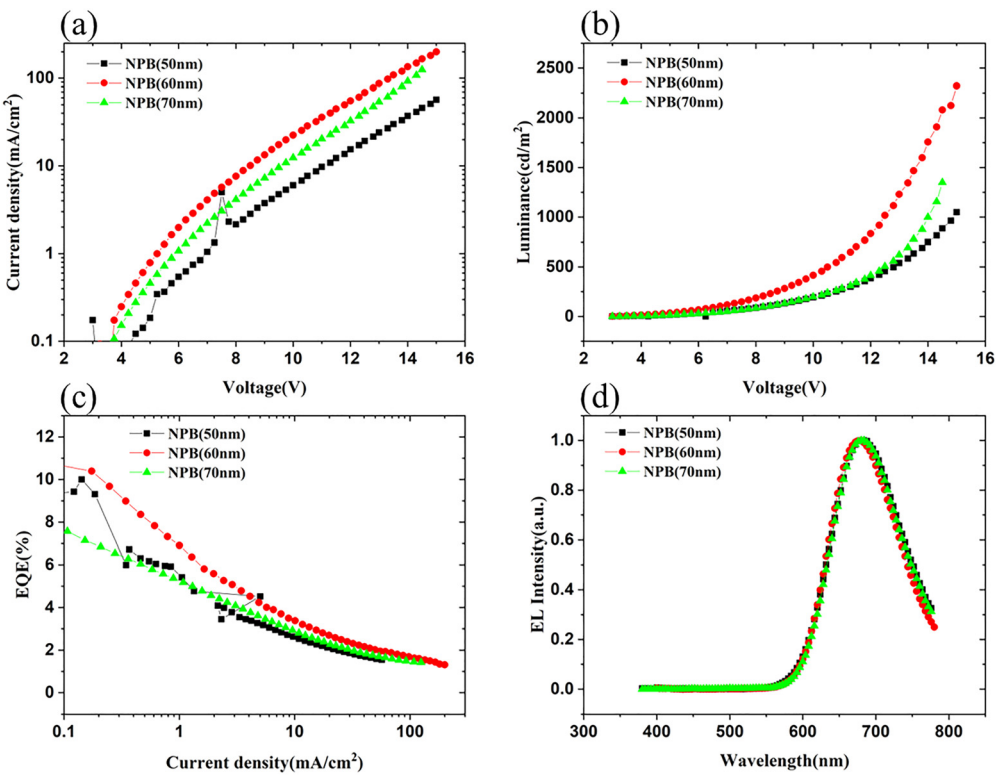

Fig. 12 Optoelectronic performance of NIR OLEDs with varying NPB thicknesses: (a) *J–V* characteristics, (b) *L–V* curves, (c) EQE–*J* curves, and (d) EL spectra.

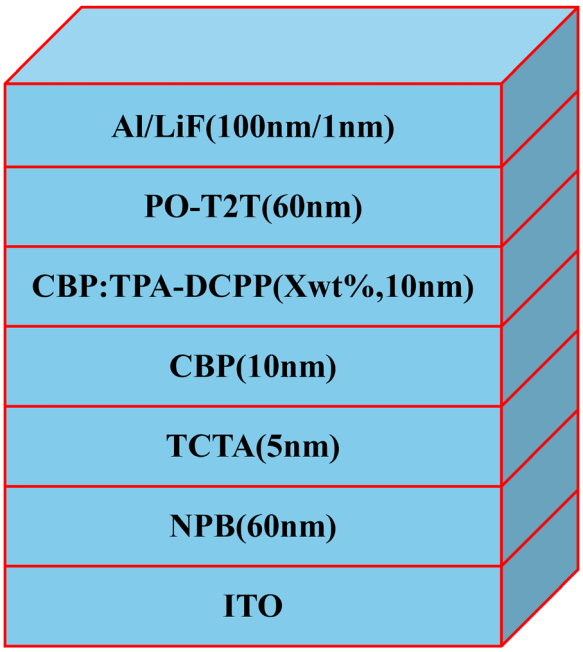

Fig. 13 Schematic diagrams of device structures with different doping concentrations.

correspondingly increasing. However, when the doping concentration is further increased to 20 wt%, the EQE decreases to 11.7%, and the luminance drops to 1737 cd m^{-2}. This reduction is attributed to the shortened intermolecular distance between TPA-DCPP molecules at high doping levels, which intensifies intermolecular interactions and suppresses efficient energy transfer, thereby lowering exciton utilization efficiency. Additionally, excessive guest loading can promote non-radiative processes such as triplet–triplet annihilation (TTA), leading to further efficiency loss.[28]

Table 5 Summary of optoelectronic characteristics of near-infrared OLEDs at different doping concentrations

TPA-DCPP (wt%)	L_{max} (cd m^{-12})	EQE_{max} (%)	Turn on voltage (V)	EL peak (nm)
5	1813	7.36	2.9	656
10	2322	11.5	2.75	680
15	2152	15.2	2.75	700
20	1737	11.7	3.25	708

Fig. 14(d) shows that as the doping concentration increases from 5 wt% to 20 wt%, the emission peak shifts from 656 nm to 708 nm, corresponding to a pronounced redshift. This spectral shift originates from enhanced energy transfer efficiency and increased exciton formation and recombination within the emissive layer at higher doping concentrations. The summarized optoelectronic performance parameters of NIR OLEDs with different doping concentrations are presented in Table 5.

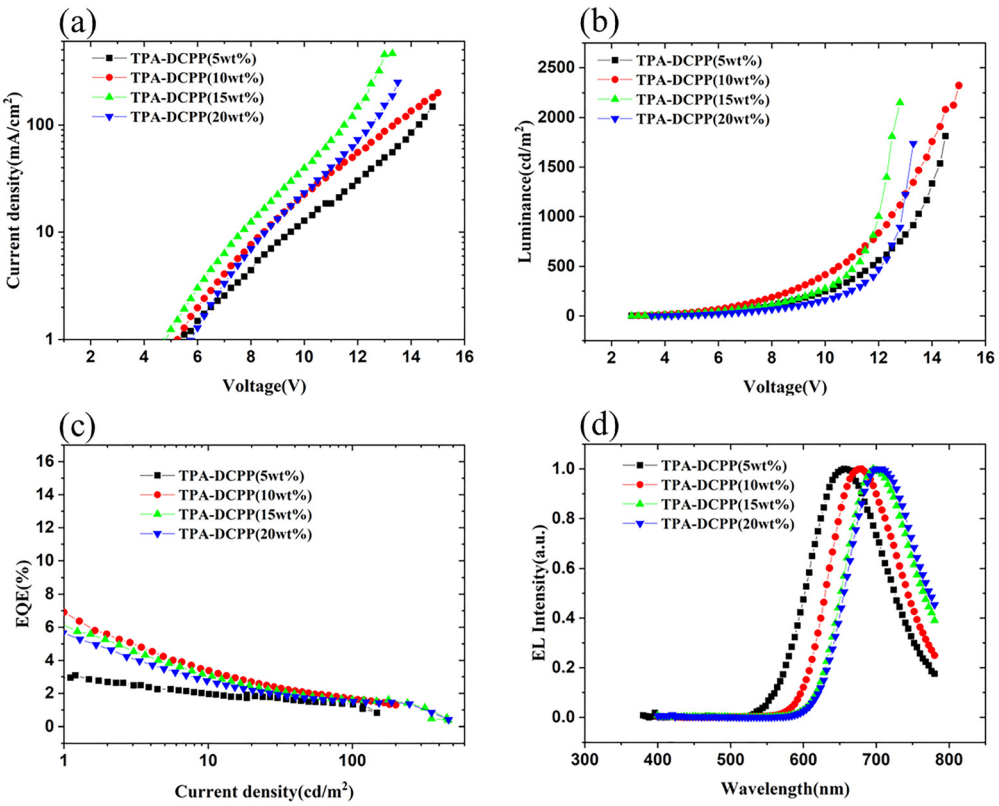

Fig. 14 Optoelectronic characteristics of near-infrared OLEDs with different guest-doping concentrations: (a) *J*–*V* curves, (b) *L*–*V* curves, (c) EQE–*J* curves, and (d) EL spectra.

These results indicate that an optimal doping concentration of 15 wt% achieves the best trade-off between exciton generation, energy transfer, and concentration quenching, resulting in the highest overall device efficiency.

2.8 Capacitance–voltage characteristics of devices with varied guest-doping concentrations

The influence of different guest-doping concentrations on device performance was further examined through capacitance–voltage (C–V) measurements, which provide direct insights into carrier injection, transport, and accumulation processes.[28] The measurements were performed at a fixed frequency of 100 Hz under an applied bias voltage (V_0) ranging from −3 V to 12 V in a non-destructive manner.

As shown in Fig. 15, the evolution of capacitance with bias can be divided into four characteristic regions, exemplified here by the device with a 15 wt% TPA-DCPP doping concentration (green solid line):

Region I ($V_0 < V_t \approx 4$ V): no carrier injection occurs, and the capacitance remains constant.

Region I ($V_0 > V_t$): once the applied voltage exceeds the threshold voltage (V_t), carrier injection begins, leading to a gradual increase in capacitance.

Region II ($V_0 \approx V_{bi} = 10$ V): carrier accumulation at the interface saturates, reaching the maximum capacitance value.

Region III ($V_0 > V_{bi}$): when the applied voltage exceeds the built-in voltage (V_{bi}), electrons and holes recombine in the emissive layer, producing electroluminescence and causing a rapid decrease in capacitance.

The extracted electrical parameters for devices with 5 wt%, 10 wt%, 15 wt%, and 20 wt% TPA-DCPP are summarized as follows: threshold voltages (V_t) of 5.1 V, 4.4 V, 4.0 V, and 4.4 V; built-in voltages (V_{bi}) of 11 V, 10 V, 10 V, and 10.8 V; and saturation capacitances of 1.2 nF, 1.4 nF, 1.55 nF, and 1.41 nF, respectively. A lower threshold voltage reflects more efficient carrier injection, while a smaller built-in voltage corresponds to a reduced turn-on voltage. Conversely, a higher saturation capacitance indicates stronger carrier accumulation at the interface.

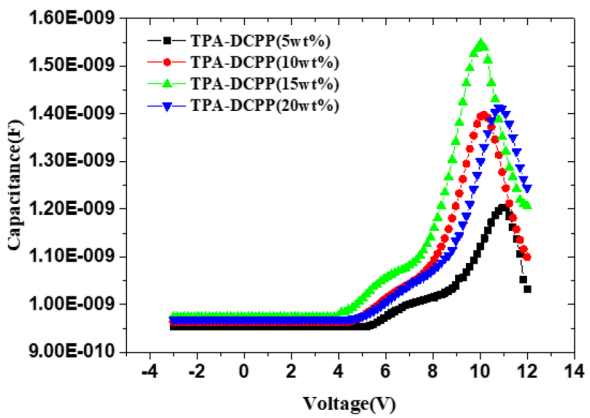

Fig. 15 Capacitance–voltage characteristics of devices with different TPA-DCPP doping concentrations at 100 Hz.

Table 6 Comparison table of optoelectronic properties and efficiencies of OLEDs based on TPA-DCPP in the near-infrared spectral range

	L_{max} (cd m^{-12})	EQE$_{max}$ (%)	Turn on voltage (V)	EL peak (nm)
This work	2152	15.2	2.75	700
29	2577	9.6	3.4	648
30	1151	4.4	3.2	674
31	<300	13.2	5.7	650
32	4691	16.4	2.9	663
33	<100	10.19	—	693
34	—	7.8	3.21	710
35	603	7.68	3.5	698
36	812.6	12.49	4.3	692

Among all devices, the 15 wt% TPA-DCPP device exhibits the highest saturation capacitance and the lowest built-in voltage, demonstrating superior carrier accumulation and the lowest turn-on voltage. These electrical characteristics are consistent with the optoelectronic performance results presented in Fig. 14, further confirming that the 15 wt% doping concentration provides the optimal charge-balance condition for high-efficiency operation.

Table 6 compares the optoelectronic performance of the TPA-DCPP-based NIR OLEDs developed in this study with previously reported results. The present device exhibits markedly higher efficiency and a lower turn-on voltage relative to earlier works. Moreover, the proposed fabrication approach offers distinct advantages in terms of low cost, structural simplicity, ease of processing, and excellent reproducibility.

3. Conclusion

In this work, a comprehensive material and device analysis was performed to investigate the optical and surface properties governing near-infrared (NIR) OLED performance. Photoluminescence (PL), transmittance, and contact-angle measurements confirmed efficient energy transfer from the interfacial exciplex to the guest emitter. By systematically optimizing the device architecture—including transport-layer thickness, guest-doping concentration, and emission-layer configuration—and analyzing carrier behavior through capacitance–voltage (C–V) characterization, a high-efficiency NIR OLED was successfully realized.

The optimized device achieved a maximum external quantum efficiency (EQE$_{max}$) of 15.2%, a peak luminance exceeding 2000 cd m^{-2}, and a low turn-on voltage while maintaining stable NIR emission. These results demonstrate the effectiveness of interfacial exciplex-mediated energy transfer in achieving balanced carrier transport and enhanced exciton utilization.

The developed device architecture offers strong potential for applications in visible light communication (VLC), night-vision and security technologies, and biomedical areas such as photodynamic therapy (PDT). In addition, this work clarifies that the exciplex is formed through a straightforward thermal evaporation and co-deposition process, without additional synthesis or complicated fabrication steps, which facilitates device fabrication and reproducibility. In addition, the high device

performance, including a maximum EQE of 15.2%, low turn-on voltage, and stable near-infrared emission, is explicitly highlighted to demonstrate the effectiveness of this method.

4. Experimental

All organic materials used in this study, including CBP, PO-T2T, TPA-DCPP, NPB, and TCTA, were commercially obtained with a stated purity higher than 99.5% and were used as received. The devices were built on glass substrates coated with indium tin oxide (ITO), which had a sheet resistance of 10 Ω and a thickness of 150 nm. ITO was used as the anode. For charge transport, 2,4,6-tris[3-(diphenylphosphinyl)phenyl]-1,3,5-triazine (PO-T2T) was utilized as the electron transport layer (ETL), and tris(4-carbazoyl-9-ylphenyl)amine(TCTA) and *N*,*N*′-di(1-naphthyl)-*N*,*N*′-diphenyl-(1,1′-biphenyl)-4,4′-diamine(NPB) were used as the hole transport layer (HTL). CBP (4,4′-bis(*N*-carbazolyl)-1,1′-biphenyl) was used as the host material due to its excellent carrier transport characteristics and also formed an exciplex at the interface with PO-T2T. 7,10-Bis(4-(diphenylamino)phenyl)-2,3-dicyanopyrazino-phenanthrene(TPA-DCPP) was used as a near-infrared dopant. Lithium fluoride (LiF) was employed as the electron injection layer (EIL), and aluminum (Al) was used as the cathode. The device structure configuration is: ITO/NPB (*X* nm, *X* = 50, 60, 70)/TCTA (5 nm)/CBP (10 nm)/CBP:TPA-DCPP (10 nm, *Y* wt%, *Y* = 5, 10, 15, 20)/PO-T2T (*Z* nm, *Z* = 50, 60, 70)/LiF (1 nm)/Al (100 nm).

The ITO-coated glass substrates were sequentially cleaned with acetone, isopropanol, and deionized water, dried using nitrogen gas, and then treated with ultraviolet-ozone for 20 minutes to eliminate surface impurities before deposition. All organic and metal layers were deposited at room temperature using thermal evaporation under high vacuum conditions ($<10^{-6}$ Torr). The deposition rate for all organic layers was maintained at approximately 1.0 Å s^{-1}. The active light-emitting area of each device was 2.5 mm × 2.5 mm. The deposition rates were monitored using a quartz crystal microbalance and calibrated using an Alpha-Step profilometer.

Measurements were conducted using an optoelectronic measurement system consisting of a source meter (Keithley-2400) and a spectroradiometer (PR-655). This system, connected to appropriate software, enabled the measurement of OLED device characteristics, external quantum efficiency-current density (EQE–*J*), luminance–voltage (*L*–*V*), and the electroluminescence spectrum (EL spectrum).

We conducted surface energy measurements (FTA-1000B) on CBP:TPA-DCPP films deposited on substrates. Deionized water (DI water) and methylene iodide (CH_2I_2) are used as test solutions for contact angle measurements, and we can calculate the surface energy using the following geometric formula:

$$\gamma_L \times (1 + \cos\theta) = 2\left(\gamma_s^p \times \gamma_L^p\right)^{\frac{1}{2}} + 2\left(\gamma_s^d \times \gamma_L^d\right)^{\frac{1}{2}} \quad (1)$$

These two values can be obtained from the contact angles of different test liquids by solving two simultaneous equations. Table 1 shows surface tension data for DI water and CH_2I_2 for polar and nonpolar solvents. Finally, an impedance analyzer (Agilent E4990A) was used to observe the effects of different bias voltages on the devices with voltage oscillation signals ranging from 100 Hz to 10 MHz.

Conflicts of interest

There are no conflicts to declare.

Data availability

We confirm that all data supporting the findings of this study are included within the manuscript. Additional raw data or materials related to the experiments, measurements, and analyses are available from the corresponding author upon reasonable request.

References

1 S. Yadav, P. Mittal and S. Negi, Recent advancements over a decade for organic light-emitting diodes: from structural diversity, role of layers, colour emission, material classification, performance improvement, fabrication to applications, *Bull. Mater. Sci.*, 2022, **45**, 109.
2 Kumar K., ''Charge transporting and thermally activated delayed fluorescence materials for OLED applications, *Phys. Chem. Chem. Phys.*, 2024, **26**, 3711.
3 K. Cheng, H. Chen, C. H. Jenkins, G. Zhang, W. Zhao, Z. Zhang, F. Han, J. Fung, M. Yang, Y. Jiang, L. Xing and Z. Cheng, Synthesis, characterization, and biomedical applications of a targeted dual-modal near-infrared-II fluorescence and photoacoustic imaging nanoprobe, *ACS Nano*, 2017, **11**, 12276–12291.
4 E. Ullah Mughal, N. Naeem, S. Fariha Kainat, A. M. Almohyawi, J. Qurban, A. Sadiq, A. Abd-El-Aziz, N. Ma, A. S. Abd-El-Aziz, A. Timoumi, Z. Moussa, S. S. A. Natto and S. A. Ahmed, Advances in the design of thermally activated delayed fluorescence materials for high-efficiency OLEDs, *J. Photochem. Photobiol., C*, 2025, **64**, 100700.
5 P. L. dos Santos, P. Stachelek, Y. Takeda and P. Pander, Recent advances in highly-efficient near-infrared OLED emitters, *Mater. Chem. Front.*, 2024, **8**, 1731.
6 M. Xu, X. Li, S. Liu, L. Zhang and W. Xie, Near-infrared organic light-emitting materials, devices and applications, *Mater. Chem. Front.*, 2023, **7**, 4744.
7 C. Li, G. Chen, Y. Zhang, F. Wu and Q. Wang, Advanced fluorescence imaging technology in the near-infrared-II window for biomedical applications, *J. Am. Chem. Soc.*, 2020, **142**, 14789–14804.
8 H.-H. Cho, S. Gorgon, G. Londi, S. Giannini, C. Cho, P. Ghosh, C. Tonnelé, D. Casanova, Y. Olivier, T. K. Baikie, F. Li, D. Beljonne, N. C. Greenham, R. H. Friend and E. W. Evans, Efficient near-infrared organic light-emitting diodes with emission from spin doublet excitons, *Nat. Photonics*, 2024, **18**, 905–912.

9 K. Lv, M. Zhang and F. Li, Efficient radical-based near-infrared organic light-emitting diodes with an emission peak exceeding 800 nm, *J. Mater. Chem. C*, 2023, **11**, 15892.
10 K. Traskovskis, A. Sebris, I. Novosjolova, M. Turks, M. Guzauskas, D. Volyniuk, O. Bevzkonvnyi, J. V. Grazulevicius, A. Mishnev, R. Grzibovskis and A. Vembris, All-organic fast intersystem crossing assisted exciplexes exhibiting sub-microsecond thermally activated delayed fluorescence, *J. Mater. Chem. C*, 2021, **9**, 4532.
11 M. Shi, J. Du, B. Zhao, B. Liu, G. Yue, H. Wang, Y. Hao, Y. Miao and K. Guo, Unveiling and refining an interfacial-resonant exciplex for ultrathin emitters in high-efficiency organic light-emitting diodes, *ACS Mater. Lett.*, 2025, **7**, 2397–2405.
12 H. Du, Y. Hao, X. Zhang, S. Zhang, Q. Liu and Z. Pang, Recent progress in high-performance thermally activated delayed fluorescence exciplexes based on multiple reverse intersystem crossing channels, *Org. Electron.*, 2025, **136**, 107159.
13 T. Huang, X. Song, M. Cai, D. Zhang and L. Duan, Improving reverse intersystem crossing in exciplex-forming hosts by introducing heavy atom effect, *ACS Mater. Lett.*, 2021, **21**, 100705.
14 J. Pu, X. Nie, D. Li, X. Peng, W. Qiu, W. Li, D. Li, G. Sun, C. Shen, S. Ji, D. Cao and S.-J. Su, Multi-sensitization strategy for high efficiency and low efficiency roll-off solution-processed single-emission-layer all-fluorescence white organic light-emitting diodes, *Chem. Eng. J.*, 2023, **471**, 144508.
15 W.-C. Cheng, M. Rong Tsai and S.-A. Chen, Creation of dual thermally activated delayed-fluorescence exciplexes in a bulk emitting layer and its interface with an electron transport layer for promoting the performance of thermally activated delayed-fluorescence organic light-emitting diodes fabricated by a solution process, *ACS Appl. Mater. Interfaces*, 2023, **15**, 31692–31702.
16 M. Sarma, L.-M. Chen, Y.-S. Chen and K.-T. Wong, Exciplexes in OLEDs: Principles and promises, *Mater. Sci. Eng., R*, 2022, **150**, 100689.
17 M. Shi, J. Du, B. Zhao, B. Liu, G. Yue, H. Wang, Y. Hao, Y. Miao and K. Guo, Unveiling and refining an interfacial-resonant exciplex for ultrathin emitters in high-efficiency organic light-emitting diodes, *ACS Mater. Lett.*, 2025, **7**, 2397–2405.
18 T.-H. Wang, B.-Y. Lan, C.-T. Tseng, C.-Y. Chuang, S.-Y. Chu and P.-C. Kao, Structure Design and Mechanism Investigation of a Yellow Phosphorescent Organic Light-Emitting Diode with Simple Structure, High Efficiency, and Low Roll-Off Efficiency, *ACS Appl. Electron. Mater.*, 2025, **7**, 2812–2821.
19 H.-Y. Yang, C.-J. Zheng, M. Zhang, J.-W. Zhao, P.-L. Zhong, H. Lin, S.-L. Tao and X.-H. Zhang, Green solution-processed thermally activated delayed fluorescence OLEDs with improved performance by using interfacial exciplex host, *Org. Electron.*, 2019, **73**, 36–42.
20 V. Jankus, C. Winscom and A. P. Monkman, The photophysics of singlet, triplet, and degradation trap states in 4,4′-N,N′-dicarbazolyl-1,1′-biphenyl, *J. Chem. Phys.*, 2009, **130**, 074501.
21 Q. Zhang, J. Jiang, Z. Xu, D. Song, B. Qiao, S. Zhao, S. Wageh and A. Al-Ghamdi, The recombination zone adjusted by the gradient doping of TPA-DCPP for efficient and stable deep red organic light emitting diodes, *RSC Adv.*, 2021, **11**, 24436.
22 P. Liu, B. Huang, L. Peng, L. Liu, Q. Gao and Y. Wang, A crack templated copper network film as a transparent conductive film and its application in organic light-emitting diode, *Sci. Rep.*, 2022, **12**, 20494.
23 D. Lee, M. S. Song, Y. Hyeok Seo, W. W. Lee, Y. Woo Kim, M. Park, Y. Ji Shin, S. J. Kwon, Y. Jeon and E.-S. Cho, Highly transparent red organic light-emitting diodes with AZO/Ag/AZO multilayer electrode, *Nanomaterials*, 2024, **14**, 385.
24 J. Marques Dos Santos, D. Hall, B. Basumatary, M. Bryden, D. Chen, P. Choudhary, T. Comerford, E. Crovini, A. Danos, J. De, S. Diesing, M. Fatahi, M. Griffin, A. Kumar Gupta, H. Hafeez, L. Hämmerling, E. Hanover, J. Haug, T. Heil, D. Karthik, S. Kumar, O. Lee, H. Li, F. Lucas, C. Frank Ross Mackenzie, A. Mariko, T. Matulaitis, F. Millward, Y. Olivier, Q. Qi, I. D. W. Samuel, N. Sharma, C. Si, L. Spierling, P. Sudhakar, D. Sun, E. Tankelvičiūtė, M. Duarte Tonet, J. Wang, T. Wang, S. Wu, Y. Xu, L. Zhang and E. Zysman-Colman, The golden age of thermally activated delayed fluorescence materials: design and exploitation, *Chem. Rev.*, **124**(no. 24), 2024.
25 M. Colella, A. Danos and A. P. Monkman, Identifying the factors that lead to PLQY enhancement in diluted TADF exciplexes based on carbazole donors, *J. Phys. Chem. C*, 2019, **123**, 17318–17324.
26 S. Ahadzadeh, S. Brebels, W. Maes and W. Deferme, Strategies for advancing near-infrared organic light-emitting diodes: innovations in luminescent materials, device architectures, fabrication methods, and applications, *Adv. Funct. Mater.*, 2025, **35**, 2419599.
27 Y.-H. Mao, M.-K. Hung, S.-T. Chung, S. Sharma, K.-W. Tsai and S.-A. Chen, Interacting emission species among donor and acceptor moieties in a donor-grafted polymer host/TADF-guest system and their effects on photoluminescence and electroluminescence, *ACS Appl. Mater. Interfaces*, 2024, **16**(44), 60715–60731.
28 S. W. Kang, D.-H. Baek, B.-K. Ju and Y. Wook Park, Green phosphorescent organic light-emitting diode exhibiting highest external quantum efficiency with ultra-thin undoped emission layer, *Sci. Rep.*, 2021, **11**, 8436.
29 S. Wang, X. Yan, Z. Cheng, H. Zhang, Y. Liu and Y. Wang, Highly efficient near-infrared delayed fluorescence organic light emitting diodes using a phenanthrene-based charge-transfer compound, *Angew. Chem., Int. Ed.*, 2015, **54**, 13068–13072.
30 Q. Zhang, J. Jiang, Z. Xu, D. Song, B. Qiao, S. Zhao, S. Wageh and A. Al-Ghamdi, The recombination zone adjusted by the gradient doping of TPA-DCPP for efficient and stable deep red organic light emitting diodes, *RSC Adv.*, 2021, **11**, 24436–24442.
31 I. Naga Sai Manoj, D. Barah, S. Sahoo, J. Bhattacharyya and D. Ray, Enhancing the efficiency of red TADF OLED by optimizing the guest-host matrix and charge balance engineering, *Synth. Met.*, 2020, **270**, 116599.

32 Y. Sun, W. Sun, D. Zhang, J. Yin, M. Mao and L. Zhou, Deep-Red Organic Light-Emitting Diodes with Increased External Quantum Efficiency and Extended Operational Lifetime by Managing the Composition of Mixed Cohosts, *J. Phys. Chem. C*, 2023, **127**, 19378–19385.

33 Y. Yuan, Y. Hu, Y.-X. Zhang, J.-D. Lin, Y.-K. Wang, Z.-Q. Jiang, L.-S. Liao and S.-T. Lee, Over 10% EQE Near-Infrared Electroluminescence Based on a Thermally Activated Delayed Fluorescence Emitter, *Adv. Funct. Mater.*, 2017, **27**, 1700986.

34 Y. Hu, Y. Yuan, Y.-L. Shi, D. Li, Z.-Q. Jiang and L.-S. Liao, Efficient Near-Infrared Emission by Adjusting the Guest–Host Interactions in Thermally Activated Delayed Fluorescence Organic Light-Emitting Diodes, *Adv. Funct. Mater.*, 2018, **28**, 1802597.

35 S. Wang, Y. Miao, X. Yan, K. Ye and Y. Wang, A dibenzo-[a,c]phenazine-11,12-dicarbonitrile (DBPzDCN) acceptor based thermally activated delayed fluorescent compound for efficient near-infrared electroluminescent devices, *J. Mater. Chem. C*, 2018, **6**, 10129–10135.

36 H. Zhang, Y. Sun, Z. Chen, W. Wang, Q. Wang, S. Chen, Y. Xu and W.-Y. Wong, Efficient deep red and NIR OLEDs based on Ir(III) complexes fabricated by evaporation and solution processing, *Chem. Eng. J.*, 2023, **451**, 138632.

